

Article

High-Quality Cutting of Soda–Lime Glass with Bessel Beam Picosecond Laser: Optimization of Processing Point Spacing, Incident Power, and Burst Mode

Jiaxuan Liu ^{1,2}, Jianjun Yang ^{1,2,*} , Hui Chen ³, Jinxuan Li ¹, Decheng Zhang ³, Jian Zhong ² and Xinjian Pan ¹

- ¹ College of Electron and Information Engineering, University of Electronic Science and Technology of China Zhongshan Institute, Zhongshan 528402, China; liujiaxuan906@163.com (J.L.); leejinxuanya@163.com (J.L.); xinjian@163.com (X.P.)
- ² School of Optoelectronic Science and Engineering, University of Electronic Science and Technology of China, Chengdu 610054, China; zhongjian@uestc.edu.cn
- ³ South China Academy of Advanced Optoelectronics, South China Normal University, Guangzhou 510006, China; 17752332766@163.com (H.C.); 15362135441@163.com (D.Z.)
- * Correspondence: sdyman@uestc.edu.cn; Tel.: +86-0760-8831-4612

Abstract: Soda–lime glass has a wide range of applications in the fields of smart electronics, optical components, and precision originals. In order to investigate the effect of processing parameters on picosecond Bessel laser cutting of soda–lime glass and to achieve high-quality soda–lime glass cutting, a series of cutting experiments were conducted in this study. In this study, it was found that the machining point spacing, the incident laser energy, and the number of burst modes had a significant effect on the machining of the samples. The atomic force microscope (AFM) showed a better quality of roughness of the machined cross-section when the spacing of the machining points was 1 μm , a locally optimal solution was obtained when the number of burst modes was 2, and a locally optimal solution was also obtained when the incident laser power was 11.5 W. In this study, better machining quality was achieved for soda–lime glass of 1 mm thickness, with an average roughness of 158 nm and a local optimum of 141 nm.



Citation: Liu, J.; Yang, J.; Chen, H.; Li, J.; Zhang, D.; Zhong, J.; Pan, X. High-Quality Cutting of Soda–Lime Glass with Bessel Beam Picosecond Laser: Optimization of Processing Point Spacing, Incident Power, and Burst Mode. *Appl. Sci.* **2024**, *14*, 1885. <https://doi.org/10.3390/app14051885>

Academic Editor: Nikolaos G. Semaltianos

Received: 28 January 2024
Revised: 18 February 2024
Accepted: 20 February 2024
Published: 25 February 2024



Copyright: © 2024 by the authors. Licensee MDPI, Basel, Switzerland. This article is an open access article distributed under the terms and conditions of the Creative Commons Attribution (CC BY) license (<https://creativecommons.org/licenses/by/4.0/>).

Keywords: processing parameters; soda–lime glass; picosecond laser

1. Introduction

Soda–lime glass is a kind of amorphous non-crystalline material that is made of quartz sand (SiO_2), soda ash (Na_2CO_3), and limestone (CaCO_3). It is the largest producer of industrial glass components [1–4].

When using traditional metal-processing methods for processing hard and brittle materials, it is easy to break the workpiece. Moreover, there is low processing efficiency, high energy consumption, poor processing quality, and many design requirements that cannot be achieved; thus, these methods are a long-term plague and impact production via their major problems [5–7].

In recent years, ultrashort pulsed lasers have become a research hotspot in the field of processing with their advantages of high precision, non-contact, and high energy density [8–16]. Pulsed lasers based on Bessel beams are widely used in micro- and nanofabrication of hard and brittle materials, such as surface microstructuring [17,18], drilling, and microchannel fabrication [19–23]. Relevant studies have confirmed the positive impact of laser spatiotemporal shaping on the processing of glass materials [24–29]. The work of several scholars has shown that the processing parameters related to spot spacing, laser incident power, and burst mode have a significant effect on the processing quality of the samples [30–35]. Multiple groups of scholars agree that the roughness of the sample cross-section is a key indicator of the laser-cut samples [33,34,36,37].

Hoyo et al. investigated the nano-limitation of energy deposition in glass using double ultrafast Bessel pulses [20] but did not study the effect of the number of burst modes on glass processing. Mishchik et al. used an ultrafast laser Bessel beam to cut glass and sapphire, which narrowed the heat-affected zone of the cut samples and improved the sidewall quality by adjusting the energy deposition [35], but there was a lack of exploration of the machining point spacing. Shin et al. used a femtosecond laser Bessel beam to cut thin glass via internal scratching and mechanical crushing and investigated the effect of pulse energy and processing point spacing on the strength of the specimen and edge cross-section morphology [38]. However, they did not investigate the roughness of the cross-section. Liao et al. investigated the effect of laser incident power, processing point spacing, and defocus distance on quartz glass [36], but the optimal roughness of their samples was still higher than 320 nm.

This paper mainly used roughness as a measurement index. In multiple batches of experiments, processing a total of 100 pieces of cutting samples, we studied the impact of different processing parameters on the processing quality. We came up with better processing parameters and processing indicators. The average roughness of the sample with the best processing effect under the processing parameters of this paper was 158 nm, which was a significant improvement.

2. Experiments

The samples used in this paper are experimental soda–lime glass sheets with a thickness of 1 mm and a size of 50×50 mm, which are pre-processed to 15×15 mm with an error range of ± 0.2 mm before the experiment. Mechanical parameters related to soda–lime glass are shown in Table 1. The experimental device is shown in Figure 1. The positioning accuracy of the 3D mobile platform (CE4550-I-PG, HUAYI LASER, Dongguan, China) is ± 5 μ m, and the repetition accuracy is ± 2 μ m. The X-Y working table is responsible for the plane movement, and the Z direction is realized by the movement of the camera controlled by the machine tool.

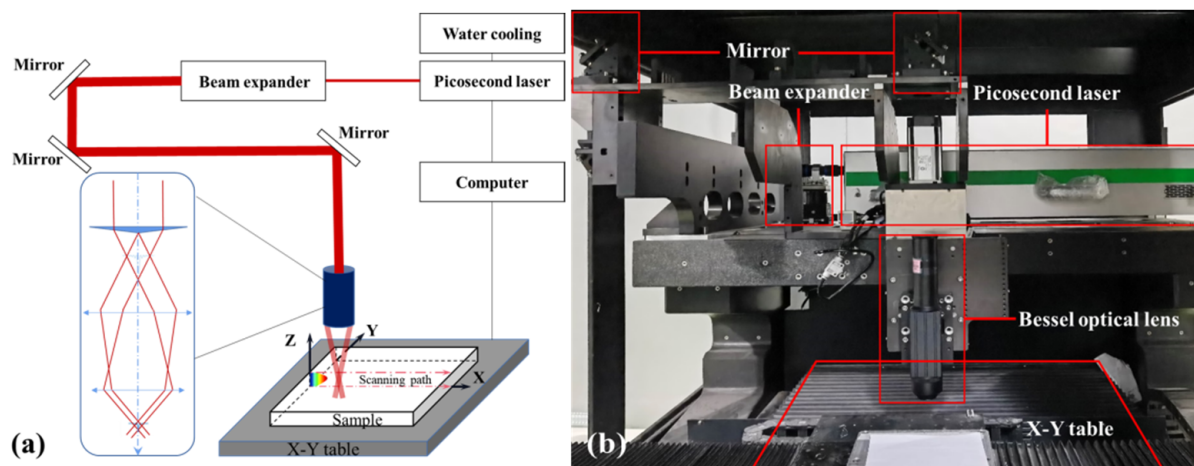


Figure 1. Schematic diagram of picosecond laser with Bessel beam cutting soda–lime glass experimental system. (a) The structure diagram of the cutting system. (b) The physical diagram of the system.

The relevant parameters of the selected picosecond laser (YP-IR-30, HUAKUAI, Jiayang, China) are shown in Table 2. The position synchronized output (PSO) mode can be used in all stages of the trajectory, including acceleration, deceleration, and curve motion, to achieve uniform pulse energy irradiation on the processed object. Burst mode is used to select multiple high-frequency sub-pulses with the same repetition rate as the seed source through a controlled optical switch to form a pulse string output.

Table 1. Table of mechanical parameters related to soda–lime glass.

Mechanical Properties	Standard Values
Density	2.2 g/cm ³
Poisson’s ratio	0.14~0.17
Thermal conductivity (20 °C)	1.4 W/m °C
Mohs hardness	7
Refractive index	1.45845
Coefficient of thermal expansion	5.4 × 10 ^{−7}
Young’s modulus	72,000 MPa
Specific heat capacity (20~350 °C)	670 J/Kg °C

Table 2. Table of parameters related to processing systems.

Parameters Related to Processing Systems	Standard Values
Laser operating frequency	50 kHz~1000 kHz
Pulse width	15 ps
Maximum output power	30 W
Wavelength	1064 nm
Positioning accuracy of the platform	±5 μm
Repetition accuracy	±2 μm
Scaling factor of telescope system	8
Refractive index of the axial cones	1.45

Picosecond laser outputs laser through the laser beam expanding mirror to obtain a radius of 3 mm Gaussian beam and Gaussian beam through the Bessel lens to obtain the Bessel beam. In this paper, the Bessel lens internal selection of the base angle α was 5°, refractive index was $n = 1.45$ for the axial cones, and the main Bessel beam cone angle θ was calculated using Equation (1) as follows:

$$\theta = \arcsin(n \times \sin\alpha) - \alpha \tag{1}$$

The primary Bessel beam produced the secondary Bessel beam by using a telescope system with a scaling factor $M = 8$ (4f system). The cone angle φ , the diameter D , and the length l of the secondary Bessel beam were calculated by the following equations:

$$\varphi = \arctan(\tan(\theta) \times M) \tag{2}$$

$$D = 4.8096/k\sin(\theta) \tag{3}$$

$$l = \omega_0/M\tan(\theta) \tag{4}$$

where $\omega_0 = 3$ mm is the radius of the beam waist of the incident Gaussian beam, and k is the wave number of the medium.

The intensity distribution of the secondary beam can be calculated by Equation (5):

$$I = I_0 \frac{z}{l} J_0^2(4.8096r/D) \exp(-2z^2/l^2) \tag{5}$$

where J_0 is the 0th-order Bessel function, and I_0 is the incident laser energy.

The Bessel spot diagram is shown in Figure 2a, where the center spot and the surrounding interference ring together form the Bessel spot. The Bessel spot energy score was filamentary, its distribution in air was simulated using COMSOL Multiphysics 6.0, and the results are shown in Figure 2b.

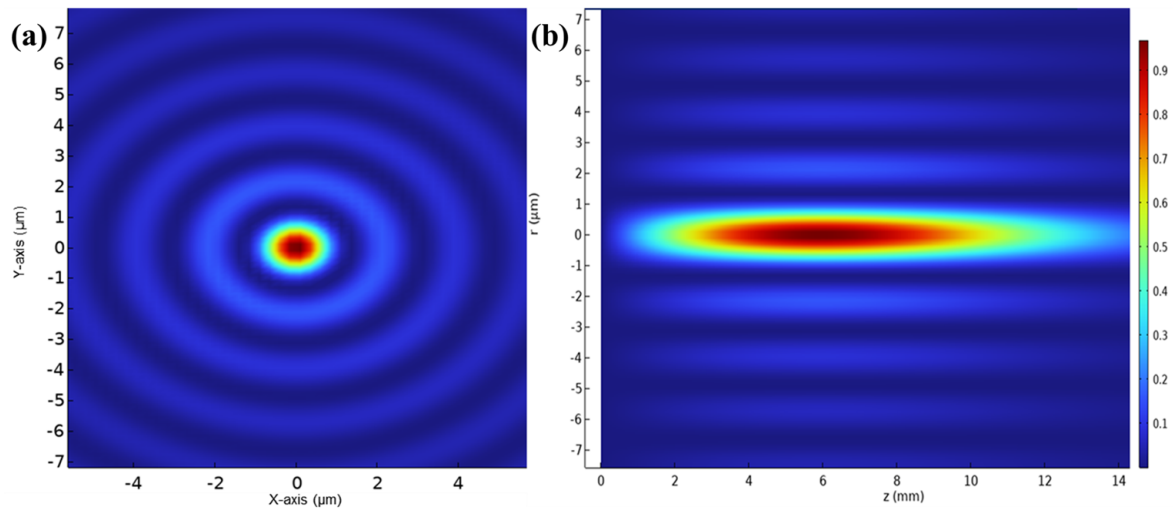


Figure 2. Schemes of Bessel beam simulation results. Picosecond laser with Bessel beam cutting soda–lime glass experimental system. (a) The structure diagram of the cutting system. (b) The physical diagram of the system.

In this paper, the cut section of soda–lime glass and the top ablation holes were observed using a metallurgical microscope (BX51M, OLYMPUS, Tokyo, Japan). The partial morphology of the glass cross-section was characterized using a scanning electron microscope (SEM-VEGA3, TESCAN, Brno, Czech). The surface morphology and roughness of the cross-sections were observed using the atomic force microscope (AFM-DSM14049BF-1, Bruker, Billerica, MA, USA). The detection of breaking strength was realized by using a pressure tester (NK-50, AIGU, Zhongshan, China).

The picosecond pulsed laser wavelength is 1064 nm, and the fixed frequency is 100 kHz. In this paper, the cutting first utilized the picosecond laser with Bessel beam to vertically incident the soda–lime glass surface. The beam was focused inside the samples. Due to the long depth of focus of the Bessel beam, the beam covered the entire cross-section of the samples. The cutting was realized along the path by moving the X-Y platform, and the different processing point spacings produced different processing aperture morphology. Then, the stresses were applied to the samples on the two sides of the processing aperture path, as shown in Figure 3a, which induced the small-aperture cracks to expand and complete the sample separation. The maximum detection range of the AFM was $100 \times 100 \mu\text{m}$. Using the maximum range, the cross-section was sampled four times, as shown in Figure 3b. The average roughness of the four samples was used to characterize the cutting effect of the entire sample cross-section.

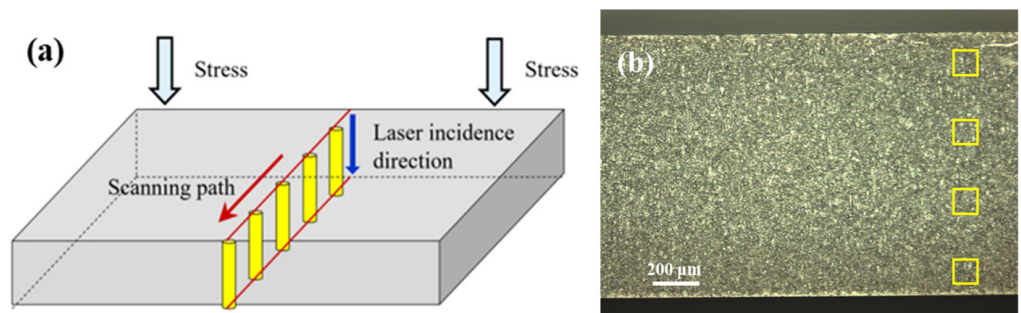


Figure 3. Schemes of sample separation and sample cross-section. (a) Scheme of sample separation force application. (b) Scheme of sample cross-section and the yellow boxes in the figure indicate the area tested by AFM.

3. Results and Discussion

In the experiment, soda–lime glass with a thickness of 1 mm was cut using a picosecond Bessel beam, and the effects of the processing point spacing, the incident laser energy, and the burst mode on the average roughness of the cut cross-section and breaking strength were analyzed.

3.1. Influence of Processing Point Spacing on Cutting Quality

The cutting results of different processing point spacing are shown in Figure 4 with a 100 kHz pulse-repetition frequency. The laser incidence at the morphology of a straight line of micropores was melt sputtering; when the processing point spacing was 1 μm , as shown in Figure 4a, micropores were connected to form an ablation groove. When the processing point spacing was more than 2 μm , the micropores were separated. When the processing point spacing was 4 μm , the micropores were more widely spaced, and cracks formed around the micropores. The microporous area is shown in Figure 4d.

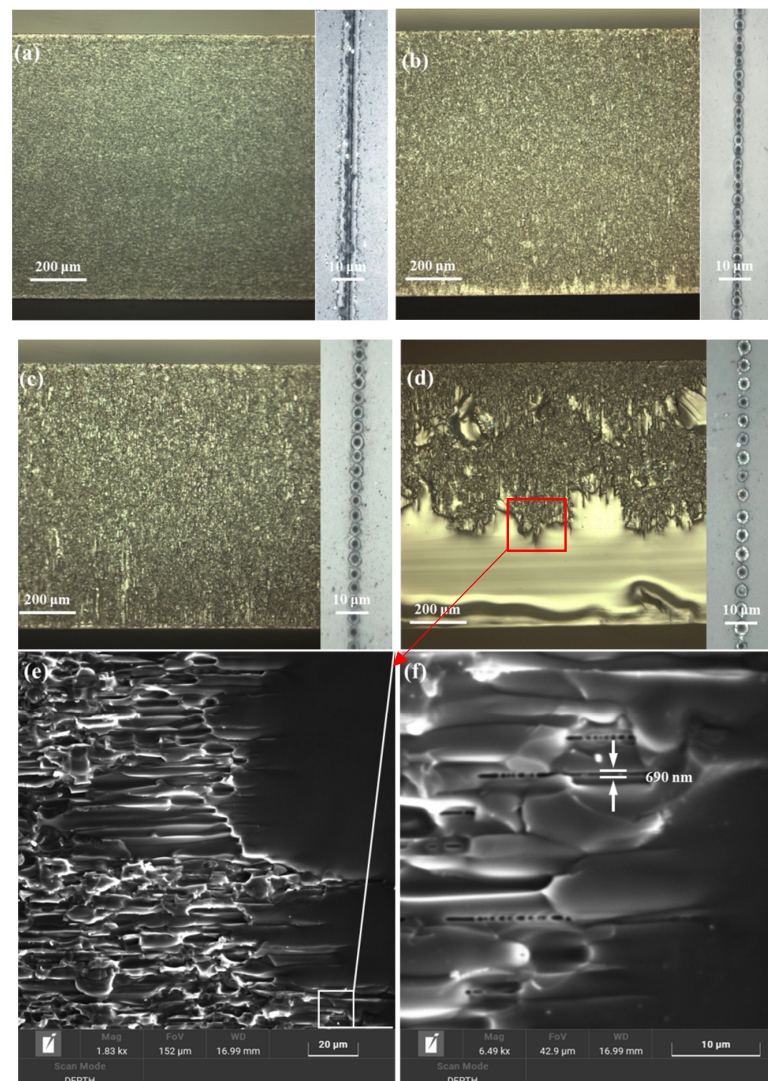


Figure 4. Diagrams of the samples with different processing point spacings and local SEM scans at a laser re-frequency of 100 kHz, an incident laser power of 11.5 W, and burst mode of 2. (a–d) represent the cross-section and the upper surface of the samples with processing point spacing of 1–4 μm , respectively, and (e,f) represent the SEM schemes of the edges of the modified layer at the processing point spacing of 4 μm .

The cross-section roughness increased with the increase in the machining point spacing, and the uniformity of ablation further decreased when the point spacing was 3 μm versus 4 μm and above. The unaltered region increased with the machining spacing of 4 μm , which made the sample separation difficult. As shown in Figure 4d under the magnification of 1.83 k and Figure 4e under the magnification of 6.49 k in the SEM picture, a series of intermittent laser ablation cavities could be observed in the cross-section of soda–lime glass. Further, a series of cavities constituted the nanochannels, with ablation diameters of about 690 nm, and the area between the nanochannels was obviously insufficient for modification. Similar nanochannels were also found at point spacings less than 4 μm . Still, the distance between submicron channels decreased when the processing point spacing was too small to improve the observation difficulty. When the point spacing was 1 μm , the affected areas of submicron channels overlapped, and no obvious channel morphology could be observed.

Roughness characterization of the sample cross-sections produced by different machining point spacings are shown in the results in Figure 5a below, where the roughness increases with increasing machining point spacing, with a relatively large roughness in the region of the sample near the middle, which was in line with the trend of the Bessel beam energy with the Z-axis used in this experiment. When the point spacing was 1 μm , the roughness difference between the regions was not obvious, and as the point spacing increased, the regions of the sample cross-section showed different modified morphology, and the difference in roughness between the regions became larger. The difference in average roughness between regions 2 and 3 reached 157 nm at 4 μm .

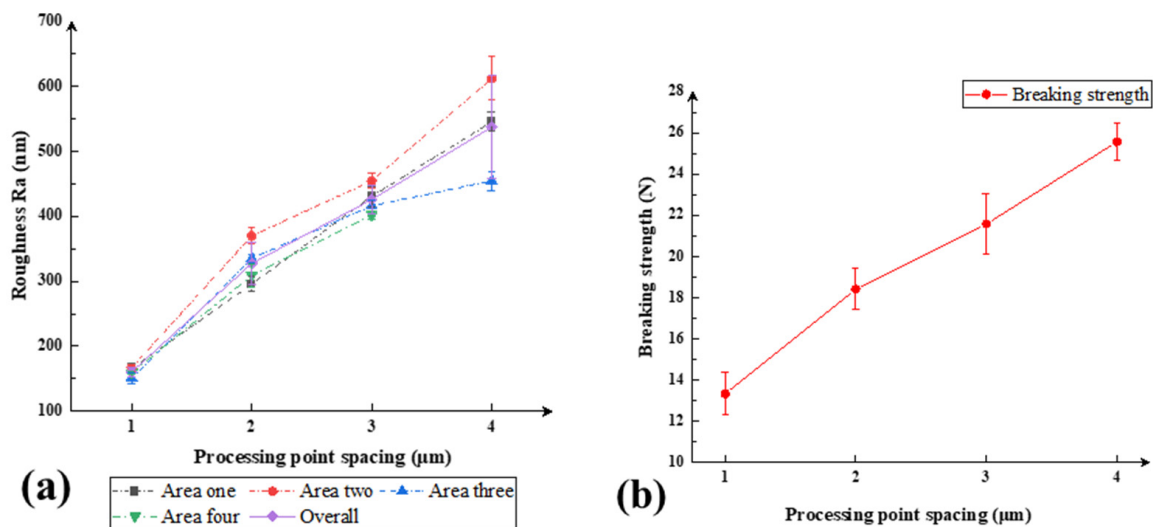


Figure 5. (a) Scheme of variation in cross-section roughness with processing point spacing with an incident laser power of 11.5 W and burst mode of 2. (b) Scheme of variation in breaking strength with processing point spacing with an incident laser power of 11.5 W and burst mode of 2.

In summary, the optimal processing quality was achieved when the processing point spacing was 1 μm and the overall modification was uniform. Samples with different processing point spacings were tested in terms of breaking strength using a hand-pressure mechanical testing system, and the variation in stress with laser processing point spacing is shown in Figure 5b.

The increase in point spacing led to a similar increase in the unmodified region, and the required stress in the samples increased due to the increase in the unmodified region. Combined with Figure 4, it can be seen that the point spacing increases, the submicron channel spacing increases, the unmodified area between the channels increases, and the influence of the lobes increases, which is the main reason for the increase in sample roughness. Roughness and breaking strength followed the same trend as the point spacing variation.

3.2. Influence of Incident Laser Power on Cutting Results

The incident laser power affects the intensity distribution of the Bessel beam. The effect of different laser incident powers on the machining quality was investigated in this section. The processing point spacing was 1 μm , the number of burst modes was 2, and the defocus distance was adjusted to cover the whole cross-section. As shown in Figure 6a, there was ablation non-uniformity in the cross-section; when the incident energy was greater than 11.5 W, the excessive laser incident energy led to crystallization of the material in the machining region, which improved the roughness of the cross-section.

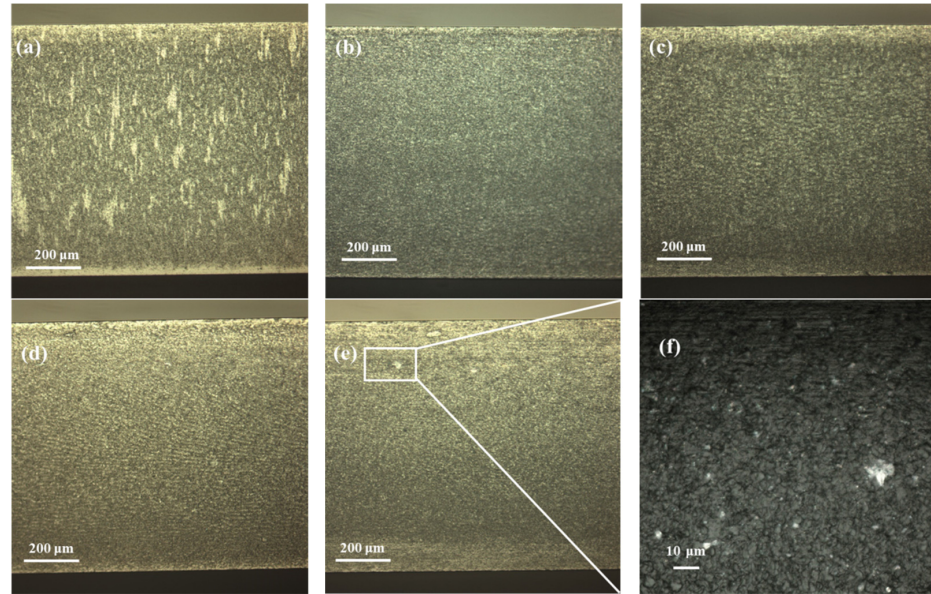


Figure 6. Diagrams of the samples at different laser incident powers when the processing point spacing was 1 μm and the burst mode was 2. (a–e) represent the cross-sections at different laser incident energies, and (f) represents the enlarged pattern of the location of the local ablation crystals when the laser incident power was 19.01 W.

The roughness of the sample cross-section was characterized with regard to different energies, and the results are shown in Figure 7a below.

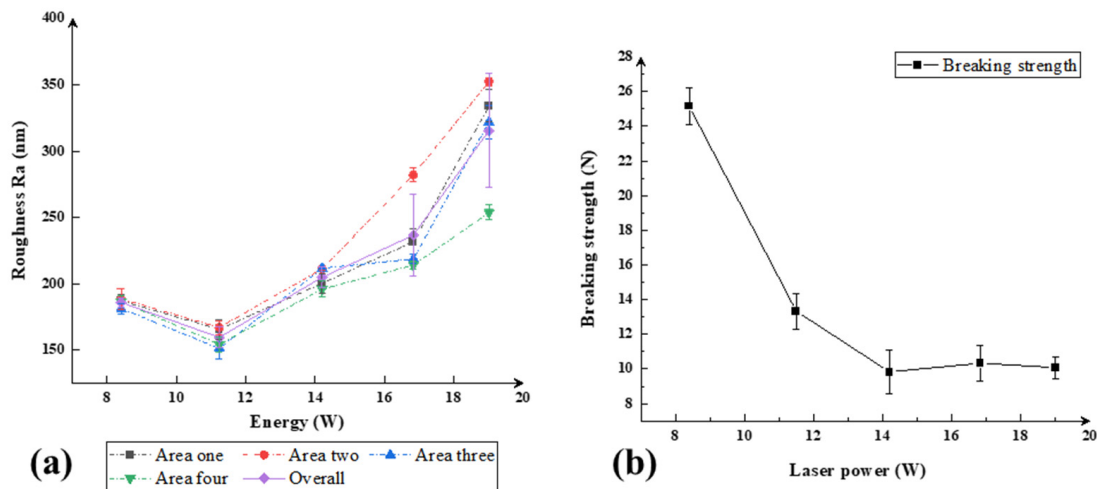


Figure 7. (a) Schemes of the variation in the sample cross-section roughness with the laser incident power for a processing point spacing of 1 μm and burst mode of 2. (b) Schemes of the variation in the breaking strength with the laser incident power for a processing point spacing of 1 μm and burst mode of 2.

The results of different power roughness detections are shown below: when the incident power was 11.5 W, the average roughness was the lowest, and the ablation was the most uniform; when the incident energy was less than this value, the ablation was not uniform and the roughness was relatively high; when the incident energy was higher than 11.5 W, the roughness of the cross-section increased further with the increase in the incident energy, and the roughness uniformity of the cross-section decreased. The standard deviation of roughness decreased when the incident energy was higher than 16 W. The average roughness of the cross-section was the lowest, and the standard deviation of roughness decreased with the increase in incident energy. Also, the standard deviation of the average roughness increased.

This recrystallization phenomenon in regions with large Bessel beam energy distributions increased the roughness of the region. We agreed that locally changed electron densities resulting in several electrical potentials coupled with high local temperatures were the likely causes of this phenomenon. As shown in Table 3, at laser injection powers of 16.83 W and 19.01 W, the maximum difference in roughness in different regions reached 68 nm and 98.67 nm, respectively. As a result, this paper hypothesizes that with a further increase in laser injection power, the internal crystallization increases subsequently, leading to a further increase in the roughness difference between different regions.

Table 3. Table of average roughness of cross-section and maximum difference in the regions for different incident powers.

Incident Laser Power (W)	Average Roughness of Cross-Section (nm)	Maximum Difference in the Regions (nm)
8.4	185.92	7.33
11.5	159.58	15.67
14.2	204.83	13.33
16.83	236.58	68
19.01	315.5	98.67

The breaking strength of laser incident power was characterized, and the results are shown in Figure 7b.

As shown in Figure 7b, with a laser frequency of 100 kHz, a processing point spacing of 1 μm , and a laser injection power of 8.4 W, the modification was incomplete, and the breaking strength was larger than 20 N. When the power was increased, the main flap energy of the Bessel beam was increased, and the modification area increased. When the laser injection power was 11.5 W, the modified layer completely covered the whole cross-section, and the breaking strength was significantly reduced, and when the power was further increased, the breaking strength was maintained near 10 N.

3.3. Influence of the Number of Burst Modes Processed on Cutting Results

Keeping the repetition frequency of the laser at 100 kHz and the energy at 11.5 W, the laser-cut samples were examined with the number of burst modes of 1, 2, 3, 4, and 5, respectively, and the results are shown in Figure 8. The concentration of energy in a single pulse results in relatively severe ablation of the sample cross-section near the upper surface area and incomplete modification of the sample near the lower surface area, as well as the appearance of a diagonal pattern. The overall modification was most uniform and effective when the number of burst modes was 2. After the first sub-pulse in the pulse train acts on the material surface, a large number of free electrons are generated due to ionization. As a result, the above factors led to significant changes in the optical properties of the material surface. After the first sub-pulse, the optical properties of the material surface changed. Therefore, when a second sub-pulse was applied after a certain pulse delay, the energy of the second sub-pulse was redistributed. This changed the light-absorption process, which in turn affected the electron density distribution. As the number of burst modes was further

increased, the energy distributed by individual pulses decreased, producing the effect of inadequate modification [22].

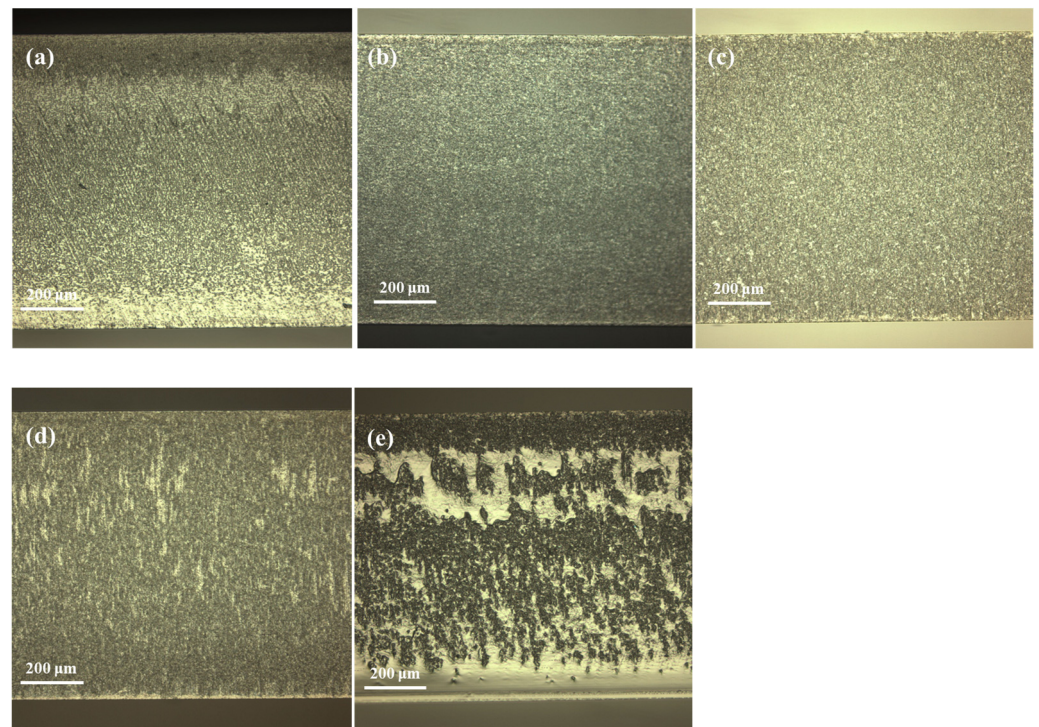


Figure 8. Diagrams of the sample cross-section for different burst mode numbers with 1 μm spacing and 11.5 W laser incident power. (a–e) represent cross-sections of the samples for burst mode numbers of 1–5, respectively.

The cross-sectional retexturing varied as the number of burst modes increased, and the higher the number of burst modes, the larger the area of inhomogeneous retexturing, as shown in Figure 8 below.

The morphology of local AFM for other sample cross-sections with burst modes 1, 2, 3, 4, and 5 were examined, as shown in Figure 9.

It can be observed through the local topography that there were more un-modified areas when the number of burst modes was 1; the overall modification was the most uniform and fine when the number of burst modes was 2; when the number of burst modes was 3, due to the decrease in the energy contained in the individual pulses, there were localized un-modified areas, which were reflected in the image by the increase in the height of the highest protrusion in the modified area and the appearance of the sticky area. When the number of burst modes was 4, the sticky area of the un-modified area was further enlarged, and when the number of burst modes was 5, there were blocky areas of the unmodified area. The peak heights of the samples showed an overall increasing trend starting with burst mode 2.

The roughness of the cross-section of the sample was examined using AFM, and the results of the variation in roughness with the number of burst modes are shown in Figure 10a.

The roughness of the cross-section of the samples was examined by using AFM, and the results of the variation of roughness with the number of burst modes are shown in Figure 10a. The optimum results were obtained with the number of burst modes of 2, with an average roughness of 158 nm, and when the number of burst modes was increased, the roughness was also increased. At burst mode number 3, the roughness of the sample cross-section was increased slightly, but the overall modification was relatively uniform, and the roughness of different areas did not differ much. With a burst mode number of 4, areas near the incidence plane (area) had better texture modification than other areas. The

inner region of the sample was more affected by the increase in the number of burst modes, and the increase in roughness was noticeable. When the number of burst modes was 5, the energy distribution of each sub-pulse was smaller, and the modified layer in the incident region was also affected by this. The modification was incomplete, which produced the phenomenon of increased roughness. Also, the overall roughness was higher with the number of burst modes of 5.

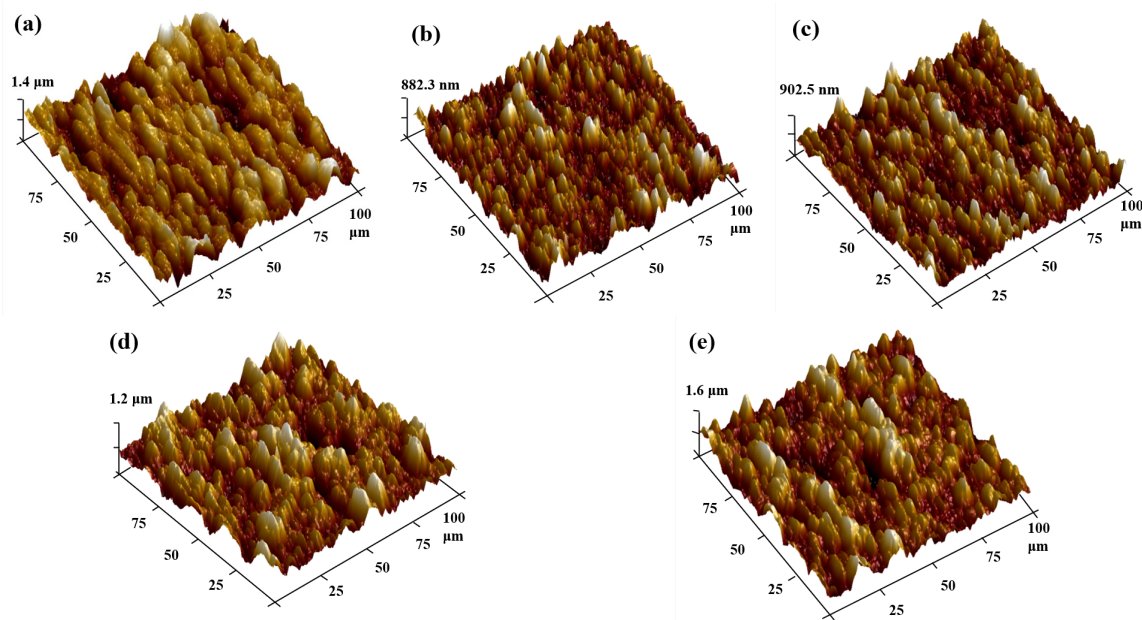


Figure 9. Schemes of the local AFM morphology of the sample cross-section at different number of burst mode with a processing point spacing of 1 μm and a laser incident power of 11.5 W. (a–e) represent the local AFM morphology of the samples for burst mode numbers of 1–5, respectively.

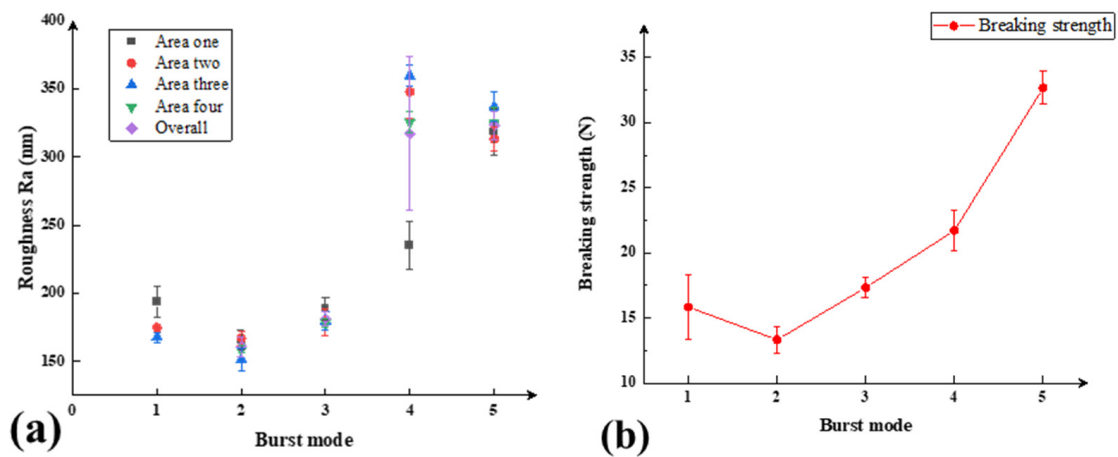


Figure 10. (a) Scheme of the local AFM morphology of the sample cross-section with different numbers of burst modes with a processing point spacing of 1 μm and laser incident power of 11.5 W. (b) Scheme of breaking strength at different numbers of burst modes with a processing point spacing of 1 μm and laser incident power of 11.5 W.

The variation in breaking strength with the number of burst modes for the laser injection power of 11.5 W at the processing point spacing of 1 μm is shown in Figure 10b.

As shown in Figure 10b, it can be seen that when the number of burst modes was 2, the breaking strength of the samples was the smallest, and when the number of burst modes was further increased, the breaking strength also became larger. The trend of the

stress with the change of burst mode was consistent with the trend of the change in the roughness, and the reforming of the reformed area affected the breaking strength and the roughness of the sample cross-section at the same time.

4. Conclusions

In this paper, cutting experiments were carried out on soda–lime glass using different laser-processing parameters, and a series of characterization tests were carried out on the samples. In this study, the effect of different processing point spacings on the cross-sectional quality of the samples was first investigated. We found that when the point spacing is large, the sample fracture is mainly caused by the extension of cracks between the processing points, the Bessel beam produces high-aspect-ratio nanochannels when performing the modification, and the energy absorption mainly occurs in the main flap. The results of the roughness characterization indicate that the overall processing quality is best when the processing point spacing is 1 μm . Secondly, the effect of different laser injection energies on the cross-sectional quality of the samples was investigated in this paper, and the most suitable incident laser power for this experiment was obtained as 11.5 W. The increase in both processing point spacing and laser injection power resulted in greater differences in the roughness of different areas of the samples. Combined with the data analysis, the point spacing was a greater factor in the overall cross-section roughness when cutting could be achieved. Then, the laser processing quality was investigated with regard to different numbers of burst modes, and it was found that the best processing quality was obtained for the burst mode number of 2. It was hypothesized from other articles that this variation was due to the fact that the first pulse produces plasma consisting of free electrons and holes or ions that decayed into self-trapped excitons and color cores. These defects increase the absorption efficiency of the second pulse. When the number of burst modes is further increased, the energy distributed by a single laser pulse decreases, resulting in non-uniform local ablation modification, which affects the processing quality of the cross-section.

When the sample was incompletely modified, the roughness and breaking strength had the same trend, as shown in Sections 3.1 and 3.3, and when the modification was more complete, the breaking strength was stabilized at about 10 N.

In this study, the processing index of roughness was practically improved by changing the corresponding processing parameters. In this experiment, when the processing laser frequency was set to 100 kHz, the laser power was 11.5 W, the processing point spacing was 1 μm , and the number of burst mode was 2, the soda–lime glass achieved excellent processing results, realizing an average roughness of 158 nm and a local minimum roughness of 141 nm. It was proved that the mastery and reasonable use of processing parameters had obvious effects on improving the processing quality of the samples.

Author Contributions: J.L. (Jiaxuan Liu) and J.Y. designed this project and carried out most of the experiments and data analysis. H.C. and D.Z. performed part of the experiments and helped with discussions during manuscript preparation. J.L. (Jiaxuan Liu) revised the paper. J.L. (Jinxuan Li), J.Z. and X.P. gave suggestions on project management and provided helpful discussions on the experimental results. X.P. supported the equipment and materials for the experiments. All authors have read and agreed to the published version of the manuscript.

Funding: This research was funded by the National Key R&D Program of China (No. 2018YFB0407100), the Natural Science Foundation of China (No. 62005041, No. 62241502), the Natural Science Foundation of Guangdong Province (No. 2018A030310662), and the Guangdong Provincial Department of Education Key Fields Special Project (No. 2022ZDZX3040).

Institutional Review Board Statement: Not applicable.

Informed Consent Statement: Not applicable.

Data Availability Statement: The original contributions presented in the study are included in the article, further inquiries can be directed to the corresponding author.

Conflicts of Interest: The authors declare no conflicts of interest.

References

1. Kartopu, G.; Oklobia, O.; Tansel, T.; Jones, S.; Irvine, S. A facile photolithography process enabling pinhole-free thin film photovoltaic modules on soda-lime glass. *Sol. Energy Mater. Sol. Cells* **2023**, *251*, 112112. [[CrossRef](#)]
2. Kuehnappel, S.; Severin, S.; Kersten, N.; Harten, P.; Stegemann, B.; Gall, S. Multi crystalline silicon thin films grown directly on low cost soda-lime glass substrates. *Sol. Energy Mater. Sol. Cells* **2019**, *203*, 110168. [[CrossRef](#)]
3. McMahon, S.; Chaudhari, A.; Zhao, Z.; Efstathiadis, H. Textured (111) crystalline silicon thin film growth on flexible glass by e-beam evaporation. *Mater. Lett.* **2015**, *158*, 269–273. [[CrossRef](#)]
4. Rojas, L.; Norarat, R.; Napari, M.; Kivistö, H.; Chienthavorn, O.; Whitlow, H. Lithographic fabrication of soda-lime glass based microfluidics. *Nucl. Instrum. Methods Phys. Res. Sect. B Beam Interact. Mater. At.* **2013**, *306*, 296–298. [[CrossRef](#)]
5. Li, K.; Chen, M.; Lin, Y.; Li, Z.; Jia, X.; Li, B. A novel adversarial domain adaptation transfer learning method for tool wear state prediction. *Knowl.-Based Syst.* **2022**, *254*, 109537. [[CrossRef](#)]
6. Gao, Y.; Chen, Y. Sawing stress of sic single crystal with void defect in diamond wire saw slicing. *Int. J. Adv. Manuf. Technol.* **2019**, *103*, 1019–1031. [[CrossRef](#)]
7. Zhou, W.; Su, H.; Dai, J.; Yu, T.; Zheng, Y. Numerical investigation on the influence of cutting-edge radius and grinding wheel speed on chip formation in sic grinding. *Ceram. Int.* **2018**, *44*, 21451–21460. [[CrossRef](#)]
8. Wang, J.; Fang, F.; An, H.; Wu, S.; Qi, H.; Cai, Y.; Guo, G. Laser machining fundamentals: Micro, nano, atomic and close-to-atomic scales. *Int. J. Extrem. Manuf.* **2023**, *5*, 012005. [[CrossRef](#)]
9. Soltani, B.; Hojati, F.; Daneshi, A.; Azarhoushang, B. Simulation of laser ablation mechanism of silicon nitride by ultrashort pulse laser. *Procedia CIRP* **2019**, *82*, 208–213. [[CrossRef](#)]
10. Moorhouse, C. Advantages of picosecond laser machining for cutting-edge technologies. *Phys. Procedia* **2013**, *41*, 381–388. [[CrossRef](#)]
11. Neuenschwander, B.; Kramer, T.; Lauer, B.; Jaeggi, B. Burst mode with ps-and fs-pulses: Influence on the removal rate, surface quality, and heat accumulation. In Proceedings of the Laser Applications in Microelectronic and Optoelectronic Manufacturing (LAMOM) XX, San Francisco, CA, USA, 9–12 February 2015; pp. 79–92.
12. Zhu, H.; Zhang, Z.; Xu, J.; Ren, Y.; Zhu, Z.; Xu, K.; Wang, Z.; Wang, C. A numerical study of picosecond laser micro-grooving of single crystalline germanium: Mechanism discussion and process simulation. *J. Manuf. Process.* **2021**, *69*, 351–367. [[CrossRef](#)]
13. Molinuevo, J.; Rodríguez-Vidal, E.; Quintana, I.; Morales, M.; Molpeceres, C. Experimental investigation into ultrafast laser ablation of polypropylene by burst and single pulse modes. *Opt. Laser Technol.* **2022**, *152*, 108098. [[CrossRef](#)]
14. Jia, X.; Li, K.; Li, Z.; Wang, C.; Chen, J.; Cui, S. Multi-scan picosecond laser welding of non-optical contact soda lime glass. *Opt. Laser Technol.* **2023**, *161*, 109164. [[CrossRef](#)]
15. Han, S.; Yu, H.; He, C.; Zhao, S.; Ning, C.; Jiang, L.; Lin, X. Laser slicing of 4h-sic wafers based on picosecond laser-induced micro-explosion via multiphoton processes. *Opt. Laser Technol.* **2022**, *154*, 108323. [[CrossRef](#)]
16. Wang, M.; Mei, W.; Wang, Y. Simulation of femtosecond laser ablation sapphire based on free electron density. *Opt. Laser Technol.* **2019**, *113*, 123–128. [[CrossRef](#)]
17. Ren, Y.; Cheng, L.; Tu, X.; He, K.; Ye, Y.; Tao, Y.; Ren, X. Precise preparation of quartz pendulous reed by using picosecond laser modification assisted wet etching. *Opt. Laser Technol.* **2023**, *163*, 109341. [[CrossRef](#)]
18. Kuriakose, A.; Chiappini, A.; Sotillo, B.; Britel, A.; Aprà, P.; Picollo, F.; Jedrkiewicz, O. Fabrication of conductive micro electrodes in diamond bulk using pulsed bessel beams. *Diam. Relat. Mater.* **2023**, *136*, 110034. [[CrossRef](#)]
19. Dudutis, J.; Pipiras, J.; Stonys, R.; Daknys, E.; Kilikevičius, A.; Kasparaitis, A.; Račiukaitis, G.; Gečys, P. In-depth comparison of conventional glass cutting technologies with laser-based methods by volumetric scribing using bessel beam and rear-side machining. *Opt. Express* **2020**, *28*, 32133–32151. [[CrossRef](#)]
20. Meyer, R.; Jacquot, M.; Giust, R.; Safioui, J.; Rapp, L.; Furfaro, L.; Lacourt, P.-A.; Dudley, J.M.; Courvoisier, F. Single-shot ultrafast laser processing of high-aspect-ratio nanochannels using elliptical bessel beams. *Opt. Lett.* **2017**, *42*, 4307–4310. [[CrossRef](#)]
21. del Hoyo, J.; Meyer, R.; Furfaro, L.; Courvoisier, F. Nanoscale confinement of energy deposition in glass by double ultrafast bessel pulses. *Nanophotonics* **2020**, *10*, 1089–1097. [[CrossRef](#)]
22. Wang, H.; Zhao, K.; Shen, H.; Yao, Z. Experimental study on direct fabrication of micro channel on fused silica by picosecond laser. *J. Manuf. Process.* **2020**, *55*, 87–95. [[CrossRef](#)]
23. Lopez, J.; Niane, S.; Bonamis, G.; Balage, P.; Audouard, E.; Hönninger, C.; Mottay, E.; Manek-Hönninger, I. Percussion drilling in glasses and process dynamics with femtosecond laser ghz-bursts. *Opt. Express* **2022**, *30*, 12533–12544. [[CrossRef](#)]
24. Dudutis, J.; Stonys, R.; Račiukaitis, G.; Gečys, P. Bessel beam asymmetry control for glass dicing applications. *Procedia CIRP* **2018**, *74*, 333–338. [[CrossRef](#)]
25. Liao, K.; Wang, W.; Mei, X.; Cui, J.; Li, M.; Li, X. An analytical model to predict the sizes of modified layer in glass with femtosecond bessel beam. *Optik* **2019**, *185*, 232–241. [[CrossRef](#)]
26. Hu, S.; Xia, X.; Gai, B.; Liu, D.; Cai, X.; Lou, M.; Li, X.; Guo, J. Laser-induced multiphoton and collisional ionizations in sodium-argon mixture. *J. Lumin.* **2020**, *225*, 117370. [[CrossRef](#)]
27. Ji, L.; Yan, T.; Ma, R. Ionization behavior and dynamics of picosecond laser filamentation in sapphire. *Opto-Electron. Adv.* **2019**, *2*, 190003.
28. Jedrkiewicz, O.; Minardi, S.; Couairon, A.; Jukna, V.; Selva, M.; Di Trapani, P. Plasma absorption evidence via chirped pulse spectral transmission measurements. *Appl. Phys. Lett.* **2015**, *106*, 231101. [[CrossRef](#)]

29. Bergner, K.; Seyfarth, B.; Lammers, K.; Ullsperger, T.; Döring, S.; Heinrich, M.; Kumkar, M.; Flamm, D.; Tünnermann, A.; Nolte, S. Spatio-temporal analysis of glass volume processing using ultrashort laser pulses. *Appl. Opt.* **2018**, *57*, 4618–4632. [[CrossRef](#)] [[PubMed](#)]
30. Sun, M.; Eppelt, U.; Hartmann, C.; Schulz, W.; Zhu, J.; Lin, Z. Damage morphology and mechanism in ablation cutting of thin glass sheets with picosecond pulsed lasers. *Opt. Laser Technol.* **2016**, *80*, 227–236. [[CrossRef](#)]
31. Xiong, S.; Wang, R.; Tao, H. Ultrafast laser micromachining the ultra-low expansion glass-ceramic: Optimization of processing parameters and physical mechanism. *J. Eur. Ceram. Soc.* **2021**, *41*, 5990–5999. [[CrossRef](#)]
32. Wen, Q.; Chen, J.; Huang, G.; Cui, C.; Mu, D. Dependence of monocrystalline sapphire dicing on crystal orientation using picosecond laser bessel beams. *Micromachines* **2023**, *14*, 772. [[CrossRef](#)]
33. Ouchene, A.; Mollon, G.; Ollivier, M.; Sedao, X.; Pascale-Hamri, A.; Dumazer, G.; Serris, E. Roughness and wettability control of soda-lime silica glass surfaces by femtosecond laser texturing and curing environments. *Appl. Surf. Sci.* **2023**, *630*, 157490. [[CrossRef](#)]
34. Li, Z.; Wang, X.; Wang, J.; Allegre, O.; Guo, W.; Gao, W.; Jia, N.; Li, L. Stealth dicing of sapphire sheets with low surface roughness, zero kerf width, debris/crack-free and zero taper using a femtosecond bessel beam. *Opt. Laser Technol.* **2021**, *135*, 106713. [[CrossRef](#)]
35. Mishchik, K.; Chassagne, B.; Javaux-Léger, C.; Hönninger, C.; Mottay, E.; Kling, R.; Lopez, J. Dash line glass-and sapphire-cutting with high power usp laser. In Proceedings of the Frontiers in Ultrafast Optics: Biomedical, Scientific, and Industrial Applications XVI, San Francisco, CA, USA, 14–16 February 2016; pp. 91–106.
36. Liao, K.; Wang, W.; Mei, X.; Liu, B. High quality full ablation cutting and stealth dicing of silica glass using picosecond laser bessel beam with burst mode. *Ceram. Int.* **2022**, *48*, 9805–9816. [[CrossRef](#)]
37. Dudutis, J.; Zubauskas, L.; Daknys, E.; Markauskas, E.; Gvozdaitė, R.; Račiukaitis, G.; Gečys, P. Quality and flexural strength of laser-cut glass: Classical top-down ablation versus water-assisted and bottom-up machining. *Opt. Express* **2022**, *30*, 4564–4582. [[CrossRef](#)] [[PubMed](#)]
38. Shin, H.; Kim, D. Strength of ultra-thin glass cut by internal scribing using a femtosecond bessel beam. *Opt. Laser Technol.* **2020**, *129*, 106307. [[CrossRef](#)]

Disclaimer/Publisher’s Note: The statements, opinions and data contained in all publications are solely those of the individual author(s) and contributor(s) and not of MDPI and/or the editor(s). MDPI and/or the editor(s) disclaim responsibility for any injury to people or property resulting from any ideas, methods, instructions or products referred to in the content.